AGU PUBLICATIONS

JGR

Journal of Geophysical Research: Oceans

RESEARCH ARTICLE

10.1002/2014JC010329

**Key Points:**
- Most of the shoreline variability is explained by interannual variations
- Wave forcing is dominated by shorter periods
- Alongshore-averaged shoreline response at annual time scales is not significant

**Correspondence to:**
C. Pianca,
catitapianca@gmail.com

**Citation:**
Pianca, C., R. Holman, and E. Siegle (2015), Shoreline variability from days to decades: Results of long-term video imaging, *J. Geophys. Res. Oceans*, *120*, doi:10.1002/2014JC010329.

Received 21 JUL 2014
Accepted 16 FEB 2015
Accepted article online 20 FEB 2015

# Shoreline variability from days to decades: Results of long-term video imaging

**C. Pianca[1,2], R. Holman[1], and E. Siegle[2]**

[1]College of Earth, Ocean, and Atmospheric Sciences, Oregon State University, Corvallis, Oregon, USA, [2]Oceanographic Institute, University of São Paulo, São Paulo, São Paulo, Brazil

**Abstract** The present work characterizes the time-space scales of variability and forcing dependencies of a unique 26 year record of daily to hourly shoreline data from a steep beach at Duck, North Carolina. Shoreline positions over a 1500 m alongshore span were estimated using a new algorithm called ASLIM based on fitting the band of high light intensity in time exposure images to a local Gaussian fit, with a subsequent Kalman filter to reduce noise and uncertainty. Our findings revealed that the shoreline change at long times scales dominates seasonal variability, despite that wave forcing had only 2% variance at interannual frequencies. The shoreline response presented 66% of the variance at interannual scales. These results were not expected since from wave forcing it would have been expected that the shoreline response should similarly lack interannual variability, but we found it to be dominated by this scale. The alongshore-mean shoreline time series revealed no significant annual cycle. However, there are annual oscillations in the shoreline response that are coherent with wave forcing and deserves further explanations. The pier was found to have a significant influence on shoreline behavior since restricts the seasonal longshore transport between the sides, resulting in a seasonally reversing sediment accumulation. Thus, there is a significant annual peak in shoreline variability that is coherent with the annual forcing but becomes insignificant in the longshore-average.

## 1. Introduction

About two-thirds of the world's population lives in the coastal regions. These regions are important economically and socially and require enlightened management to preserve and manage their value for the future. Beaches occur on practically all coasts of the world but are inherently variable as sand is constantly shifted by waves, wind, and nearshore currents.

Erosion can reduce beaches areas and destroy houses and commercial properties along the coastlines. Thus, from the coastal management point of view, it is important to know where the shoreline is, where it has been in the past, and where it will be in the future. The location of the shoreline can be used to quantify historical erosion rates [*Moore*, 2000] and give information about the beach volume and width [*Smith and Jackson*, 1992].

Shoreline changes can occur on temporal scales that range from long-term (years, decades, and centuries), to seasonal variability that repeats on an annual cycle, to short-term (days and months, storm events) and spatial scales that span from meters for beach cusps to the many kilometers of shoreline evolution. It has commonly been assumed that coastal variability was dominated by seasonal, or summer-winter cycles [*Komar*, 1998], where summer or calm conditions are characterized by a wide berm and smooth offshore profiles, while winter or storm conditions feature narrow and steep foreshores with no berm, and sand bars that migrate offshore.

For most practical purposes, the shoreline is considered to be the key representative of the varying beach and is often the legal separation of property and the ocean. Historically, the shoreline was defined as the position of high water level (HWL) because it could be visually identified in the field by the wrack line of residual debris left by the previous high tide. With the introduction of measurement techniques such as LIDAR and GPS, the shoreline became defined on the basis of an elevation or a tidal datum, such as mean high water (MHW) [*Hapke et al.*, 2006]. The Dutch define the Momentary CoastLine (MCL) as an integrated measure of the volume of sediment within the active shoreline region [*Min V & W*, 1990], a measure that is

insensitive to details of profile shape so a better basis for coastal zone management decisions like shoreline nourishment. Thus, the shoreline definition can vary depending on the data source available and the detection technique used. A complete review of shoreline definitions is reported by *Boak and Turner* [2005]. Shoreline position is one of the most commonly monitored and generally accepted indicators of coastal change [*Morton*, 1996].

The ability to understand and predict shoreline variability has been restricted by the lack of observational data, especially over the multidecade time scales over which interannual variability has been seen in some sand bar observations [e.g., *Wijnberg and Terwindt*, 1995; *Plant et al*., 1999]. Common methods have included ground based surveys of cross-shore profiles [e.g., *Miller and Dean*, 2004; *Miller and Dean*, 2007]; vehicle-mounted GPS [e.g., *Morton et al*., 1993; *Ruggiero et al*., 1999; *Ruggiero et al*., 2003; *Yates et al*., 2009; *Hansen and Barnard*, 2010] and airborne LIDAR systems [e.g., *Sallenger et al*., 1999; *Stockdon et al*., 2002]. Yet these are manpower intensive and logistically challenging, so are expensive as a long-term solution. Similarly methods such aerial photography, satellite images, and airborne radar can cover large spatial scales, they are usually sparse in time due to prohibitive costs. GPS surveys require that survey teams go out into the field, so can only be done infrequently. However, the advance of digital imaging technologies has made it possible to collect high-frequency, long-duration images of coasts at low cost, greatly increasing the capability to monitor detailed changes in the coastal system.

The objective of this paper is to investigate a 24 year record of nearshore wave forcing and the corresponding 26 year record of daily to hourly of shoreline locations extracted from video images, characterize the space-time scales of shoreline variability, and correlate the observed shoreline changes with the wave forcing.

In the next section, we will discuss the field site and data sources for this paper, review the past literature of video-based shoreline estimation, then describe our estimation method, including quality control and confidence estimation, a comparison with ground truth data and describe the spatial and temporal variability of the wave forcing. In the following section, we will present and describe the results, presenting the data in a sense of spatial and temporal variability of the shoreline response, the relationships between the response and wave forcing and an empirical orthogonal function (EOF) analysis of shoreline patterns. We close with a discussion and conclusions.

## 2. Description of the Data Set

### 2.1. Field Data: Duck Beach, North Carolina

Duck Beach is located on the east coast of the United States, in the state of North Carolina (Figure 1) and since has been the home of the U.S. Army Corps of Engineers Field Research Facility (USACE-FRF–http://www.frf.usace.army.mil/), an important and internationally recognized coastal observatory. This beach is oriented $-20.3^{\circ}$ north-northwest of true north. The foreshore is relatively steep at 1:12.5 [*Plant and Holman*, 1997; *Holland*, 1998], flattening offshore where one or two sand bars are commonly present and vary on both annual and interannual time scales [*Alexander and Holman*, 2004]. Beach sediments are composed of fine to coarse sand [*Stauble*, 1992]. At this site, there is a research pier oriented $69.78^{\circ}$ east-northeast of true north and is considered shore normal to the beach *Miller* [1999]. The tide regime is microtidal with a semi-diurnal period and a typical tide range of 1 m. Tide data were collected from a tide gauge located at the seaward end of the FRF pier.

The wave regime is dominated during the summer time by waves approaching from the south and having an average significant wave height around 1 m. During the rest of the year, this beach commonly experiences storm conditions with waves approaching from northeast and occasional hurricanes and tropical storms with wave approach from the south. Wave data were collected from two instruments, a waverider buoy ($36^{o}11.30'$ N, $75^{o}44.60'$ W) at 17.4 m depth and an 8 m array composed of 15 pressure gauges (both instruments are shown at Figure 1). For this present study, data from the 8 m array will be used. However, this instrument became inoperative in January of 2012 and the wave time series were extrapolated with the data the waverider buoy. Other data gaps found in the 8 m array collection were also interpolated with waverider buoy data.

The video images were obtained through a system called an Argus Station which was installed on a 43 m tower overlooking the beach. The station has been in continuous operation since 1986 and has seen a

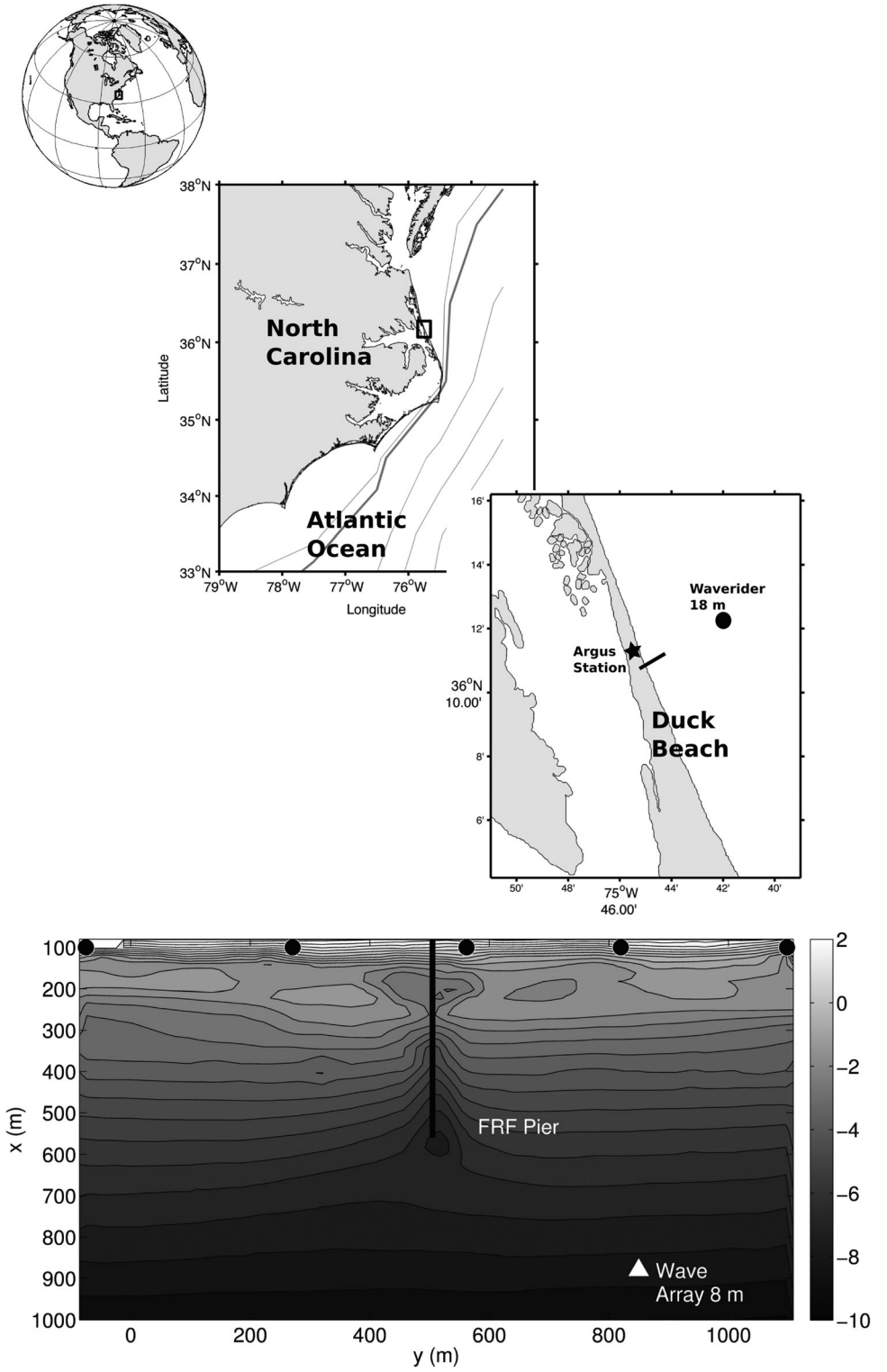


**Figure 1.** Map of Duck Beach, USA. The white triangle indicated the location of the 8 m pressure gauges and the black circle on the map is the waverider buoy at 17.4 m depth. The black line is the FRF research pier. The black star indicates the location of the video tower. (bottom) Map of the bathymetry and the black circles indicate the surveys profiles used to validate the ASLIM model.

considerable evolution in both technology and video coverage since that time [see *Holman and Stanley*, 2007, for a discussion of the nature and historical evolution of Argus data collection]. From 1986 to 1992, images were captured by videotape and post processed into useful image products. A single camera

viewed the beach to the north of the observation tower, located just to the north of pier. In 1992, data collection was automated but continued with single camera coverage until 1995 when offshore and southward-facing cameras were added, still leaving data gaps to the northeast and southeast. These were filled in 1997 with the addition of two further cameras to form a five camera set that spanned the full coastal field view. In 2005, the older analog cameras were replaced by higher-resolution digital cameras that have run since that time.

Ground control points (GCP's) within each field of view were used to determine the camera's orientation relative to the ground topography, using photogrammetric transformations of image coordinates to ground coordinates according to the method outlined in *Holland et al*. [1997].

For each camera, time exposure images (timex, averaging 2 Hz frames collected over a period of 10 min) were collected every hour of daylight. Timex images have proved to be very useful for observing submerged morphology since the wave breaking over sand bars produces white foam over these features, and also for observing variability in the shoreline since a white shore break has been shown to occur near the still water shoreline [*Plant and Holman*, 1997]. For measurement purposes, the time exposure images can be rectified into horizontal maps and converted to world coordinates using standard photogrammetry techniques [*Holland et al*., 1997].

The pixel resolution of the cameras, in the cross-range direction worsens with distance from the cameras while along-range resolution worsens as range squared [*Holman and Stanley*, 2007]. The region of interest spans from −250 to 1250 m in the alongshore direction and 70–180 m in the cross-shore (later increased to 60–180 m due to excessive erosion to the north of the pier). Camera resolution has evolved with time, especially in the earliest years of the station. The mean pixel resolution in the region of interest has varied over the 26 years from 1 to 0.5 m in the cross-shore direction, and from 3 to 1 m in the alongshore direction. These are clearly sufficient to quantify the natural shoreline variations over the record.

### 2.2. Shoreline Extraction Model

The method tested in this paper is a proxy method, based not on direct survey, but instead on imaging the shore break in Argus time exposure images and empirically relating it to a shoreline datum. It follows from a previous literature, described hereafter, to measure shoreline location from image data in order to quantify this key measure of coastal health.

*Plant and Holman* [1997], followed by *Madsen and Plant* [2001], developed a technique to exploit the white foam generated by swash motions at the shoreline in a shore-parallel band of high light intensity which is very clear on time exposure images on steep beaches. They named this band the shoreline intensity maximum (SLIM). The SLIM method will be discussed again in the next paragraphs. *Turner et al*. [2001] used a method based on color discrimination wherein the relative amount of red and blue light was used to distinguish the sand and water surfaces. They called their method the CCD Model (Color Channel Divergence). *Aarninkhof et al*. [2003] developed a method called Pixel Intensity Clustering Model that it is also based on the color difference between wet and dry beach sand but with the distinction defined by a statistical cluster analysis. Finally, *Kingston* [2003] used an artificial neural network (ANN) to differentiate wet from dry pixels and identify the shoreline position, using manually selected regions of sand and water to train the network before it was applied to an extensive image archive. Most recently, *Plant et al*. [2007] compared these four different shoreline mapping methods in each of the four different places they were developed and concluded that the shoreline detection methods provided similar results but with slightly different relative cross-shore displacements at each location, and that intertidal bathymetry estimated with any of the methods ought to be intercomparable and complementary over a wide range of geomorphic and environmental conditions.

Like the method of *Plant and Holman* [1997], the method tested in this paper is based on time exposure images that average the shore break dissipation over a period of 10 min to reveal a white band whose location can be found. This feature is apparent on steep beaches like Duck but may be less useful on flatter beaches. With more than 25 years of images to analyze, it was important to develop a method for shoreline extraction that is automated and robust.

In developing their method for extracting robust estimates of the cross-shore location of the ShoreLine Intensity Maximum from a sequence of time exposure images, *Plant and Holman* [1997] noted that simply

using the location of maximum intensity in a swash search region would return noisy results associated with small fluctuations in the shore break intensity profile. Instead, they pointed out that the results would be more robust if they fit a parabola to the intensities near the shoreline and used the maximum in the fitted function to define the SLIM position. They found the measurement error for individual shoreline estimates in a field comparison to be about 0.10 m in the vertical. This method was updated by *Madsen and Plant* [2001] who used, instead of a parabola to fit the intensities, the superposition of a quadratic and Gaussian-shaped function where the quadratic modeled the background intensity in the near-shoreline region and the Gaussian represented the intensity maximum above that background. Results were similar to *Plant and Holman* [1997], with a mean error (0.12 m in the vertical) when compared with surveys data.

Our approach will also base estimates of shoreline location on the band of high light intensity on timex images but will model the maximum as a local Gaussian but without the parabolic background profile. A second and more important change will be the implementation of a Kalman filter to reduce noise and uncertainty in the resulting time series of shoreline measurements. Kalman filters have been widely applied to coastal geophysical applications, especially in data assimilation with numerical models [*Chen et al*., 2009; *Wilson et al*., 2010], bathymetry estimation [*Holman et al*., 2013], and shoreline evolution [*Long and Plant*, 2012]. We called our method the Augmented Shoreline Intensity Maximum, or ASLIM.

### 2.3. ASLIM (Augmented ShoreLine Intensity Maxima)

The first step in the algorithm is to load the rectified time exposure image $I(x, y, t')$ for time $t'$ (primes denote a specific position x or y, or a particular time t). For each alongshore location ($y'$) in the image, the cross-shore ($x$) intensity profiles $I(x, y', t')$ were extracted. The intensities were then normalized from 0 to 1, $\hat{I}(x, y', t')$. The domain was limited to a cross-shore region of interest (ROI) that contained the possible range of shoreline variation for each profile and had a width of 110 m for the study area. Figure 2 shows an example rectified time exposure image (top) with superimposed extracted shoreline (white line) and location of example transect (black line) while the bottom plot shows the cross-shore transect of intensity (black-dotted line) and the local Gaussian shoreline fit (solid gray line). This paper will adopt the convention of offshore (positive $x$) being down and north (positive $y$) to the right in all figures to be consistent with the beach view shown in Figure 2.

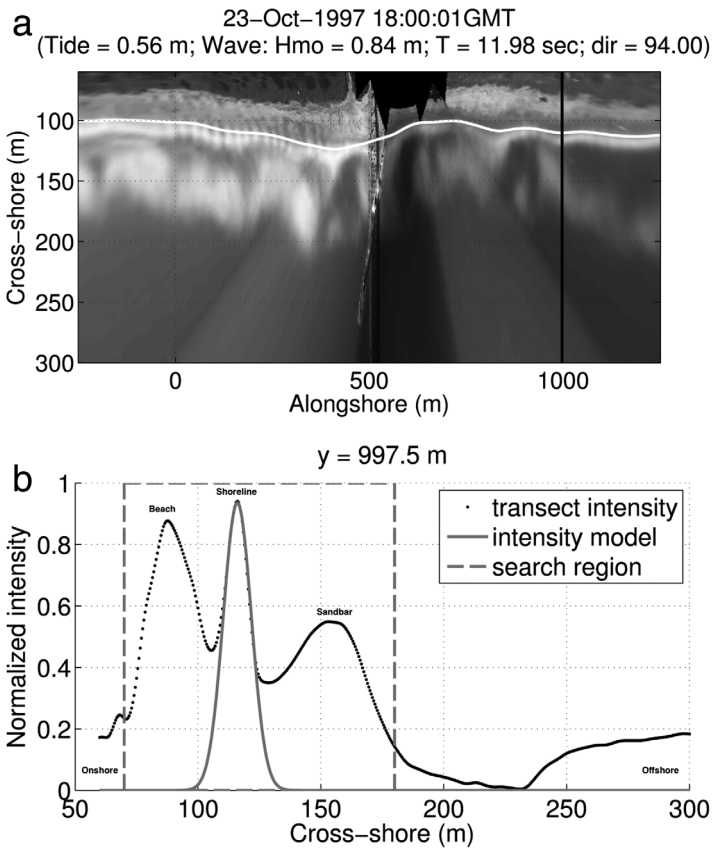


**Figure 2.** Example ASLIM position estimates (top) showing a rectified time exposure image (timex) overlain with the instantaneous shoreline (solid white line) extracted using ASLIM and the location of an example cross-shore transect (black line), while (bottom) shows the example intensity profile at y = 997.5 m (black-dotted line), the Gaussian fit (solid gray line) and the region of interest (dashed gray line). The rectified time exposure is a merged composite of data from the five cameras needed to span the domain.

To improve the fit, the search area within the ROI was restricted to the region of a local peak and adjacent slopes. The initial guess of the peak location was defined by a change of slope ($\frac{dI}{dx}$) from positive to negative, and the region of analysis spanned to the surrounding inflection points. After defining this curvature

region, a nonlinear least square fit to a Gaussian function was performed in the vicinity of the local maximum of the curvature using the function.

$$\hat{I}(x, y', t') = A * \exp\left[\frac{-(x - x_s)^2}{L}\right] \tag{1}$$

where $A$ and $L$ are the amplitude and width of the Gaussian function, respectively, and $x_s$ is the center peak location. Figure 2b shows an example of the Gaussian function fitted over the normalized intensity profile for $y = 997.5$ m.

The $A$ values were constrained to range between 0 and 1 (since the intensities were previously normalized) and the $L$ to range from 1 to 20, where 20 is a reasonable extreme standard deviation for a shore-break Gaussian [*Madsen and Plant*, 2001]. The results from the fit function were the tide-dependent shoreline position $\hat{x}_s(y, t')$, values for $A(y, t')$ and $L(y, t')$ and the variance of each estimate $(\sigma^2_{\hat{x}_s}, \sigma^2_A, \sigma^2_L)$.

Because the $\hat{x}_s$ position is dependent of the tidal level, causing daily shoreline position variations, the tidal effect was removed and results were expressed in terms of a base shoreline location, $\hat{x}_o(y, t')$:

$$\hat{x}_o(y, t') = \hat{x}_s(y, t') + \frac{z_t(t)}{\beta} \tag{2}$$

where $z_t(t)$ is the tidal elevation and $\beta$ is the foreshore slope. A climatological value of $\beta$ was chosen as 1:12.5, based on previous results by *Plant and Holman* [1997] and *Holland* [1998].

The last step is the implementation of the Kalman filter to reduce the uncertainty associated with each instantaneous measurement, some of which will be inevitably be poor due to weather conditions. The Kalman filter equation that updates our prior estimate of shoreline location is:

$$\tilde{x}_o^{(t)} = \tilde{x}_o^{(t-1)} + K(\hat{x}_o^{(t)} - \tilde{x}_o^{(t-1)}) \tag{3}$$

where $\tilde{x}_o^{(t)}$ is the new estimate, $\tilde{x}_o^{(t-1)}$ is the prior estimate, and $K$ is the Kalman filter gain that compares the credibility of the new estimate with the prior estimate and is obtained from:

$$K = \frac{P_t^-}{P_t^- + R} \tag{4}$$

$P_t^-$ is the error variance of the prior estimate, updated to time, $t$, and $R$ is the error variance of the new estimate.

According to equation (4), if the new measurement error, $R$, is much larger than the prior confidence, $P_t^-$, the Kalman filter gain ($K$) tends to zero and the new data is largely ignored, i.e., $\tilde{x}_o^{(t)} \sim \tilde{x}_o^{(t-1)}$ (see equation (3)). In contrast, if $R$ is much smaller than $P_o^{(t-1)}$, the Kalman gain ($K$) tends to one and the new estimate is trusted more, so $\tilde{x}_o^{(t)} \sim \tilde{x}_o^{(t)}$.

The value of $P$ was known at the previous time step, $t - 1$, but will have become more uncertain since then due to unmodeled natural processes. This increase in error variance is modeled as:

$$P_t^- = P_{t-1}^- + Q * \triangle t \tag{5}$$

where $Q$ is known as the process error and $\Delta t$ is the time interval since the last estimate. The last step of the process is to update $P$, the error variance of the estimate, since it has been improved by the incorporation of the new measurement. This is done by:

$$P_t^+ = (1 - K) * P_t^- \tag{6}$$

The measurement error, $R$, could be obtained from any of the confidence intervals $(\sigma^2_A, \sigma^2_L, \sigma^2_{\hat{x}_s})$ calculated for the parameters found in the least square curve fit. Initially, the value $\sigma^2_{\hat{x}_s}$ was used but proved to be unrealistically small, commonly just a few centimeters. Instead, it was assumed that the accuracy of the shoreline position would be better represented by the width of the shore break, so $R$ was taken as the value $L^2$.

The process error, $Q$ must represent the expected variability on the shoreline due to natural shoreline processes. Because shoreline change depends of the wave conditions, for example eroding during storms, the

significant wave height was taken into account for the $Q$ calculation ($Q=Q_{sh}{}^2 * H_{mo}^2$, where $Q_{sh}$ was chosen to be 2 days$^{-1}$, a value that gave the best qualitative performance in tests). A similar form was chosen by *Holman et al*. [2013] for the cBathy algorithm.

Results for the first time exposure image of the time series must be digitized manually since there is no prior seed for either finding the peak subregion or for the Kalman filter process. Since the measured shoreline was manually digitized, the error was estimated to be small ($P_{t=1}=1^2\ m^2$).

### 2.4. Data Quality

#### 2.4.1. Quality Control

The data were partitioned into subsets before and after 1997, recognizing the lack of full alongshore coverage before 1997. Over the many years of data collection, images were sometimes unusable for a variety of reasons including fog or rain. While the Kalman filter deals with quality variations, it was determined that sufficiently bad images such as foggy days should be omitted from further analysis based on objective quality control measures. Quality control was based on the error variance ($R$) which depended on the width of the Gaussian function as $L^2$. It was found that when more than 40% of the values of measured error variance in a histogram were between 350 and 400 (i.e., near the maximum value of $L = 20$ m), the images were of poor quality (rainy day, glare day, or loss of shoreline tracking) and were eliminated. For the pre-1997 Duck data, 20.20% of the data were discarded (3574 out of 17,695 shorelines extracted). After 1997, 11.02% of the data were removed (5745 out of 52,138 estimates shorelines).

A final quality control check was implemented by examination of all images and superimposed shorelines in a movie loop. It was found that under some conditions, the automatic shoreline detection would lose track of the true shoreline and track an erroneous feature, so would require a manual reseed to stay on track. Problems were usually local, spanning 50–100 m in the longshore, and could be associated with the emergence of a low-tide terrace at low tide, the presence of large amplitude beach cusps, or odd morphologies very close to the research pier (also where optical data were obstructed). For cases of persistent problems, the shoreline was redigitized (reseeded) every 4 days with ASLIM running automatically between reseeds. At final count, 3.44% of the images were reseeded, i.e., 1951 of a total of 56,791 images. Initially, alongshore locations were estimated independently. However, it was determined that alongshore smoothing of the initial estimates helped stabilize performance. Smoothing was first done using a convolution with a Hanning filter with half-power cutoff of 36 m for the early records from 1986 to 1994. However, for cases of prominent beach cusps a shorter cutoff of 16 m worked better and shorelines were redigitized from 1994 to 2012.

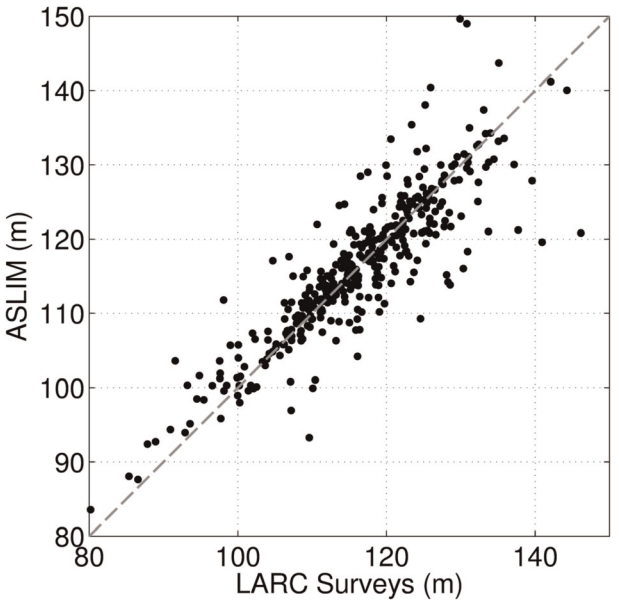


**Figure 3.** Comparison between surveys data and ASLIM model ($R^2 = 0.92$; r = 0.85 with 95% confidence intervals of 0.78 and 0.88; and slope of 0.90). The dash gray line indicates along the 1:1 relationship.

#### 2.4.2. Comparison Against Ground Truth

A comparison between ASLIM results and survey data was used to validate our shoreline model. The surveys were carried out by the FRF crew using the LARC (http://www.frf.usace.army.mil/larc/larcsystem.stm), and the data are referenced at NAV88 datum, with the shoreline located at z = 0 m. Five different alongshore profiles were chosen between 1997 and 2012, a total of 376 surveys. Figure 1 shows the location (black circles) of the five profiles. Figure 3 shows the relation between the ASLIM positions and the shoreline obtained by the surveys at the five

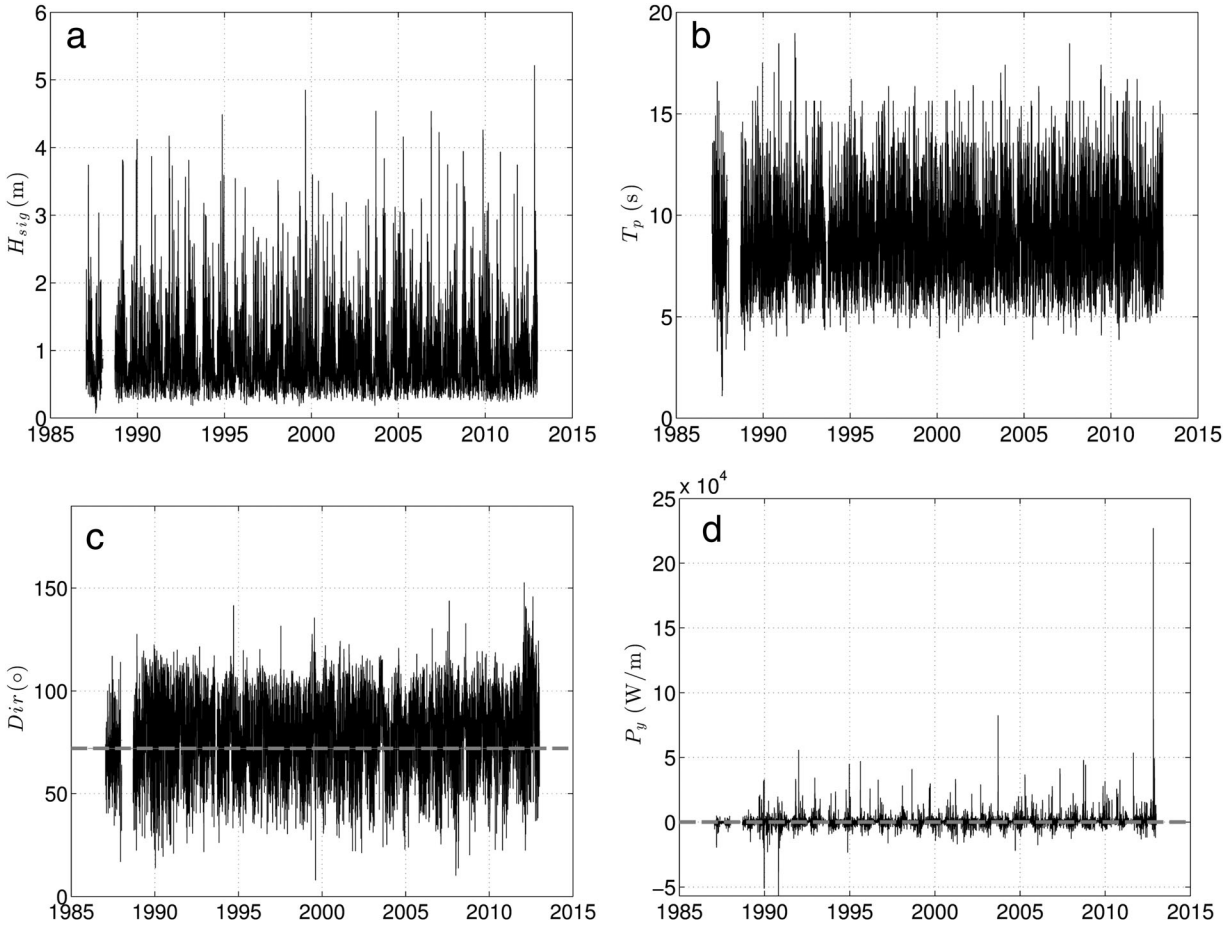


**Figure 4.** Wave conditions at Duck extracted from the FRF's 8 m pressure gauges: (top left) significant wave height (m), (top right) peak period (s), (bottom left) wave direction (degrees) and (bottom right) alongshore wave energy flux. Data gaps mostly correspond to days with no data. Positive alongshore wave energy flux corresponds to transport to north. The large spike at the end of the $P_y$ record corresponds to Hurricane Sandy.

profiles. The results obtained by the ASLIM model showed good agreement with the surveys data, with a RMSE of 5.1 m, a least square slope of 0.90 and an $R^2$ value of 0.92.

### 2.5. Analysis Methods

The following analysis will first examine the wave forcing record and then that of the corresponding shoreline response. Variability will be partitioned into four time scales: interannual cycles which corresponds with periods longer than 1 year; the annual cycle (i.e., variations over the seasons); the intra-annual cycle that corresponds with periods shorter than 12 months but longer than 20 days and the weather cycle with periods between 20 and 2 days. For both sets of data, wave forcing and shoreline response, spectral analysis was done with interpretation based on the four time scales described above. An empirical orthogonal function (EOF) analysis was applied for the shoreline response data.

### 2.6. Wave Forcing

Figure 4 shows the daily wave time series for Duck, extracted from the FRF's 8 m pressure array. Because there was no alternate source of wave direction data during the data gap from January 1988 to September 1988, the wave analysis will be restricted to the period between September 1988 and December 2012. The possible wave forcing of longshore sediment transport was represented by the alongshore component of wave energy flux, $P_y = |P| \sin(\alpha)$, where $|P| = \frac{1}{8}\rho g H_{sig}^2 c_g$, $c_g$ is the group velocity, and $\alpha$ is the wave direction, measured positive counterclockwise from shore normal ($y$ axis is positive towards north-northwest). Significant wave heights can reach values over 5 m. We also see an annual signal where lower energy waves

**Table 1.** Wave Statistics During the Period of Study Based on a Daily Wave Time Series

| Wave Parameter | Mean | Std | Max | Min | Range | Trend |
|---|---|---|---|---|---|---|
| $H_{sig}$ (m) | 0.88 | 0.55 | 5.21 | 0.18 | 5.03 | $5.7 \times 10^{-4} \pm 4.6 \times 10^{-3}$ |
| Tp (s) | 9.03 | 2.24 | 19.0 | 3.35 | 15.61 | $1.8 \times 10^{-2} \pm 9 \times 10^{-3}$ |
| Dir (deg) | 79.30 | 18.62 | 152.62 | 8 | 144.62 | $0.18 \pm 0.18$ |
| $P_y$ (W/m) | 932.49 | 4989.4 | 2.27x10$^5$ | −56881 | 2.84x10$^5$ | $59.64 \pm 15.77$ |

come from one direction in one season and a different direction and more energy later. In the wave energy flux figure, we see that $P_y$ has transport most frequently toward the north-northwest (positive direction). The average alongshore transport was 932.56 W/m with a standard deviation of 4989.4 W/m (Table 1).

Mean and standard deviations as well as 24 year trends were computed for each variable in Figure 4 and are listed in Table 1. From the table, we observe that the mean wave height is $0.88 \pm 0.55$ m (confidence limits are one standard deviation), the mean period for the region is $9 \pm 2.24$ seconds and the predominant wave direction is from east-northeast (the wave direction is based on the true north). The time series were also tested for the presence of trends (Table 1). For the wave heights, the trend was $5.7 \times 10^{-4} \pm 4.6 \times 10^{-3}$ m/yr (95% confidence intervals); for wave period, the slope was $1.8 \times 10^{-2} \pm 9 \times 10^{-3}$ s/yr; for wave direction, the trend was $0.18 \pm 0.18°$/yr and for $P_y$ the trend was $59.64 \pm 15.77$ W/yr.

The annual cycle of wave forcing data can be found by averaging values partitioned by month (Figure 5). Wave heights show a seasonal cycle and are more energetic and stormier (higher standard deviation) during fall and winter and less energetic and stormy during the spring-summer. Monthly averaged wave direction

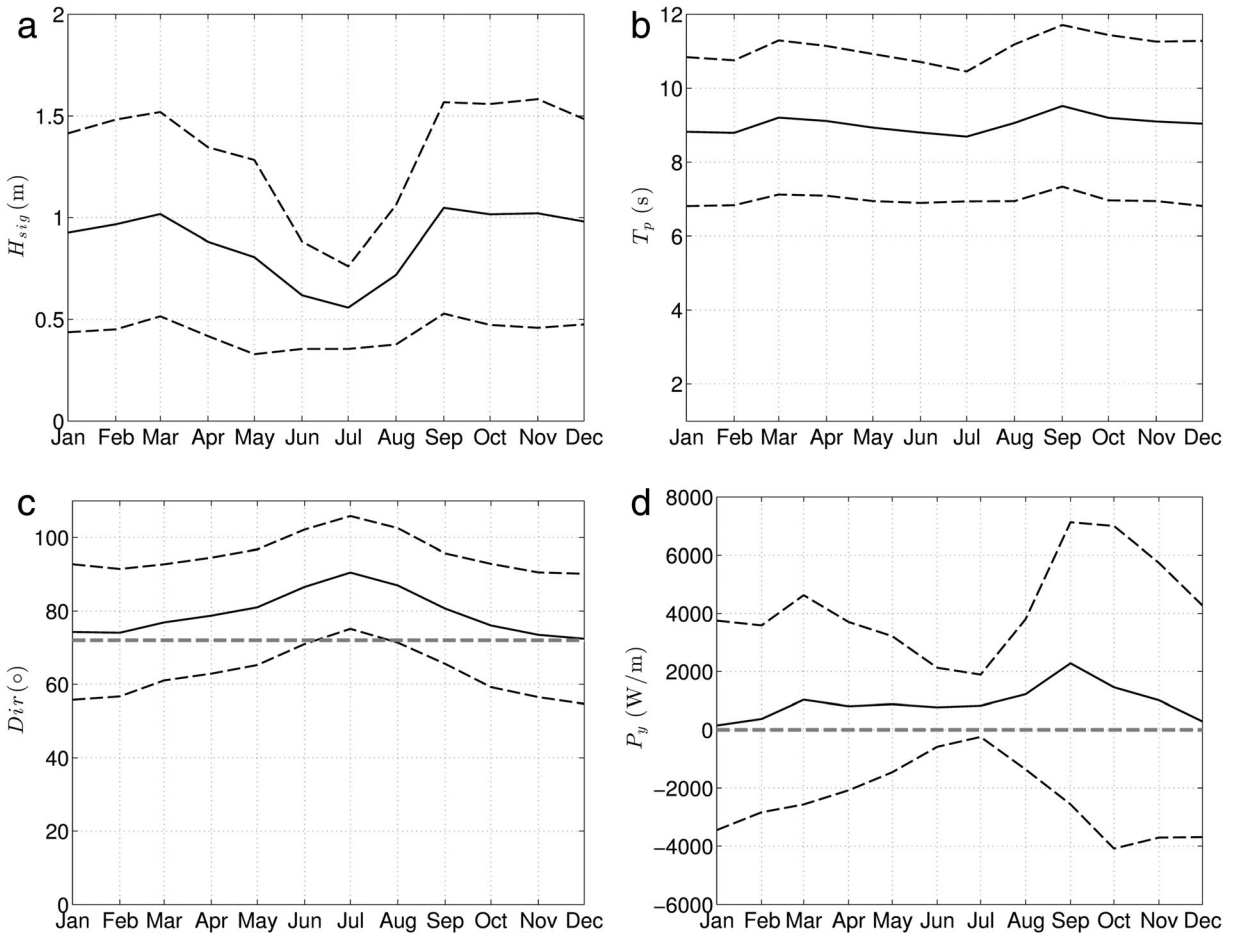


**Figure 5.** Annual signal of the wave parameters: (top left) significant wave height (m), (bottom right) wave period (s), (bottom left) wave direction (deg) and (bottom right) alongshore wave energy flux. Solid black lines show the monthly means while-dashed black lines are spaced one standard deviation away. The horizontal-dashed gray line in wave direction indicates the direction of shore normal.

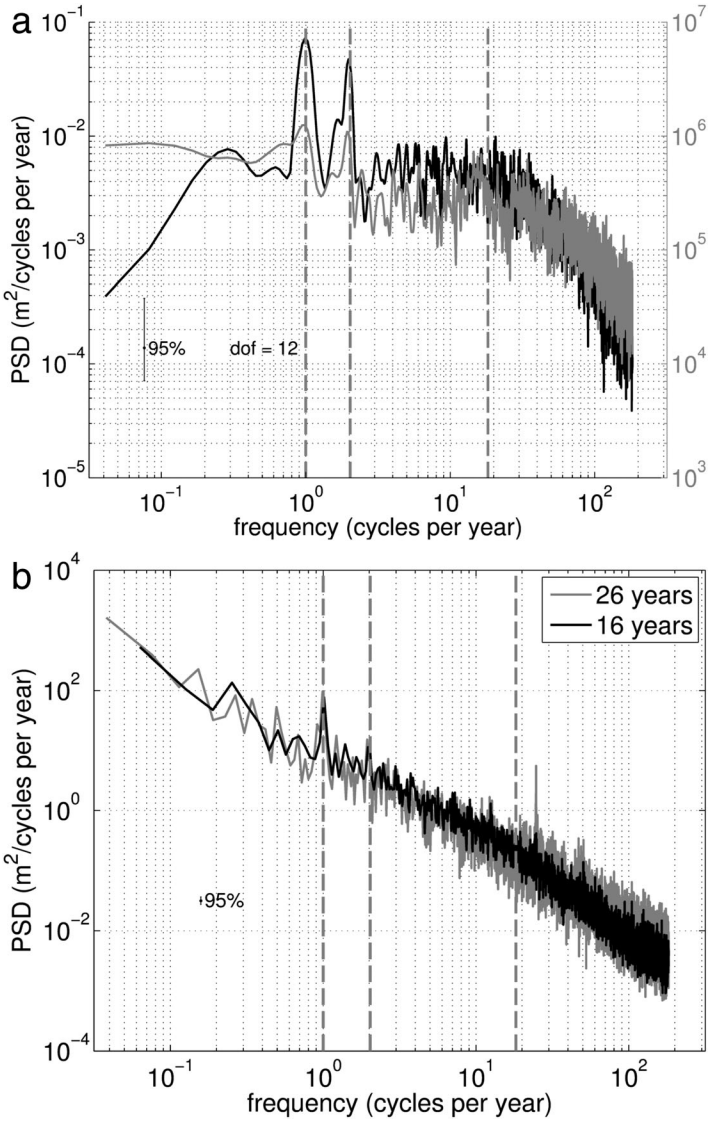


**Figure 6.** (left) The power spectral density for the wave height (black line) and alongshore wave energy flux (solid gray line). The dashed gray lines are indicative of the annual, semi-annual, and 20 days frequencies, respectively. (right) The power spectra of the base shoreline for 26 years (gray) and 16 years (black).

follows a similar cycle with wave approach coming from more southerly directions during the summer months and near shore normal through the more energetic months. Average wave periods are surprisingly uniform through the year.

This pattern is also observed in the longshore wave energy flux ($P_y$) which is directly dependent of the wave direction and wave height. The monthly averaged alongshore wave energy flux ($P_y$) is always slightly to the north, peaking during the September hurricane season when wave heights increase but approach is still commonly from the south (see the Discussion section for comments on the sensitivity of this result to the definition of beach orientation).

Figure 6 (left) shows the power spectral density (PSD) of $H_{sig}$ and $P_y$. In both cases, the peak energy lies at 1 and 2 cycles per year corresponding to the annual cycle and its first harmonic. The spectrum for $H_{sig}$ is generally flat (white) up to a frequency of 20 cycles per year (up to the weather band) before falling by about two orders of magnitude. The PSD for the alongshore wave energy flux is also fairly flat through the intra-annual band with a slight increase in the interannual.

Table 2 shows the amplitudes ($Amp=\sqrt{2Var}$) and percentages of the variance explained by each cycle for $H_{sig}$ and alongshore wave energy flux. Despite showing the lowest spectral levels, the weather cycle explains the largest fraction (roughly 2/3) of the variance for the two parameters due to the wide frequency range over which it acts (total variance in a band is the area under the spectrum in that band). The intra-annual cycle is the next-most important contributor followed by the annual and then interannual cycles.

One conclusion of this analysis is that the vast majority of variability in forcing is at annual or shorter scales with only 1–2% of the variability at interannual time scales. Under linear thinking, this would imply that the shoreline response should similarly lack interannual variability.

## 3. Shoreline Response

This section describes the results found for the shoreline response at Duck due to the wave forcing described above. Figure 10 is a space-time plot, or timestack, which shows the time dependence of shoreline deviations as a function of alongshore position. This figure will be discuss later on this section, but it is

**Table 2.** Amplitudes (Amp) and Percentages of the Variance (% Var) Associated With Each Frequency Band for the Wave Parameters: $H_{sig}$ and $P_y$

| | $H_{sig}$ | | $P_y$ | |
|---|---|---|---|---|
| Cycles | Amp (m) | % Var | Amp (W/m) | % Var |
| Interannual | 0.09 | 1.47 | 1143.4 | 2.63 |
| Annual | 0.18 | 5.38 | 515.18 | 0.53 |
| Intra-annual | 0.44 | 32.35 | 3369.60 | 22.81 |
| Weather | 0.60 | 60.79 | 6061.30 | 73.80 |

important to mention it, since shows the analysis partitions into two data sets (26 years and 16 years) that represent the full 26 year period for which data were available for $y >= 800$ m, and the 16 years of data for which better camera coverage allowed analysis over the full 1500 m alongshore distance.

In the following, we will parse the shoreline signals into the mean and deviations about the mean, then analyze both the longshore and temporal variability and their relationship to wave forcing.

Figure 7 presents a 2-D histogram of shoreline positions for the 16 year data set, where the contours represent the cumulative probability of shoreline location (percent of the time that the shoreline was landward of each contour). The influence of the pier appears to cause approximately 15 m excursion anomalies in the adjacent several hundred meters, in contrast to the original long, straight shoreline that was found prior to the FRF pier construction in 1977 (C. Mason, personal communication, 1982). The standard deviation of the shoreline distributions (not shown) was found to be surprisingly alongshore-uniform at $9 \pm 1$ m for $y < 800$ m and broadening by 2 m to the north. We also see that the shoreline is more stable to the south (narrow pdf at small $y$ value). The broader pdf to the north is associated with the typical erosive bay adjacent to the pier and a megacusp feature near $y = 1000$ that eroded away in later years (see bottom timex of Figure 10). The cumulative probability results are useful for coastal management since they show the probability that the shoreline will ever be landward of that position. Longshore variability is again emphasized, as the 2% exceedance location is 20 m further landward on the north side of the pier than to the south.

### 3.1. Temporal Variability

The time variability of alongshore-averaged shoreline position $<\tilde{x_o}>_y(t)$ is shown in Figure 8 for both data sets (26 years and 16 years). We observe that the expected annual signal is not obvious. Instead, the shoreline response appears to be dominated by interannual signals at near-decade time scales and a later trend, in contrast to the near absence of an interannual component in the forcing. The higher recent erosion rates for the 26 year data set ($y \geq 800$ only) are related to the late erosion to the north of the pier, a trend not equally seen to the south.

The shoreline trends for the 26 years and 16 year time series were found to be $-0.81 \pm 0.65$ m/yr and $-0.57 \pm 0.35$ m/yr, respectively. The slopes for both time series are negative implying general erosion. However, we observe that for some periods such as 1991–1995 and 2001–2003, the averaged-shoreline accreted by several tens of meters.

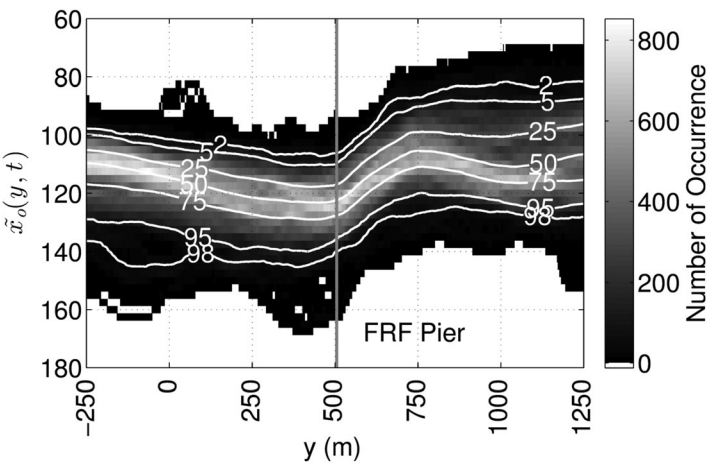


**Figure 7.** Shoreline histogram and cumulative probability distribution (white lines) for shoreline position for the 16 year data set as a function of longshore location.

The alongshore variability of the shoreline trend is shown in Figure 9. We observe again that alongshore variations are important for shoreline studies. For $y \leq 400$ m (to the south), the erosion rate is not significantly different from 0.0. However, to the north there is a steady increase in erosion rate up to a peak of 1–2 m/yr.

In the following analysis, we wish to examine the shoreline

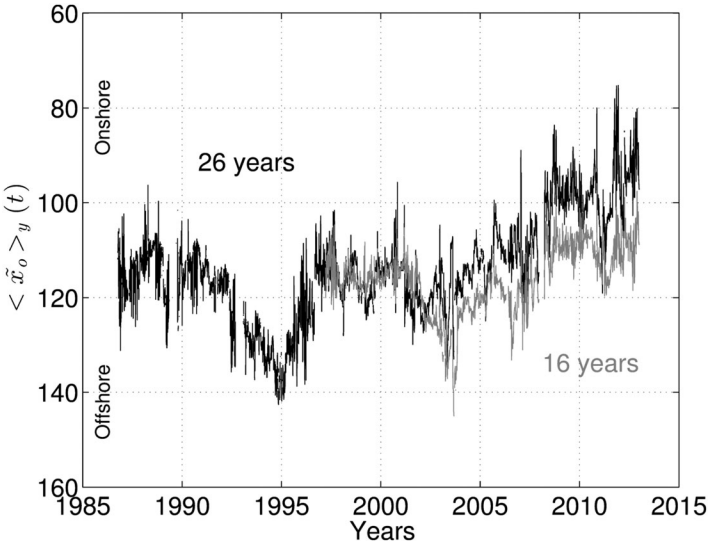


**Figure 8.** The alongshore-averaged shoreline position $<\tilde{x}_o>_y(t)$ (m) for the 26 year (black line) and 16 year (gray line) data sets.

variability about the mean shoreline. We will refer to this as shoreline deviations ($x_o'(y,t)$), obtained by:

$$x_o'(y,t) = \tilde{x_o}(y,t) - \overline{x_o}(y) \quad (7)$$

where $\overline{x_o}(y)$ is the time-mean shoreline and $\tilde{x_o}(y,t)$ are the shoreline positions as a function of time and y.

In the Figure 10, cold colors indicate a landward, or erosive position, and hot colors seaward, or accretionary, deviations of shoreline position. We observe a major signals of accretions during 1992–1995 and erosion in 2008–2012. In 2003–2004, accretion event is seen to be present at all alongshore locations while the erosion starting in 2008 is mostly limited to the north. Shifts of sediment between the north and south sides of the pier are apparent, for example in 1999 and 2002.

The average annual signal of shoreline variability was found by averaging values partitioned by month, in this case using the 16 year record to reveal the full alongshore structure (Figure 11). This figure is very informative since an annual signal is clearly evident with accumulation near the pier, first on the north side due to winter waves that arrive from the northeast causing an accumulation on the north side of the pier and erosion south side. Then in spring summer, the process is reversed with deposition on the south side under the influence of southerly waves, and erosion to the north. Thus, accretion on one side will be accompanied by erosion on the other, illustrating the influence of the pier in partially blocking alongshore transport. From this figure, we note that the region of pier influence is at least 500 m, much larger than the influence region assumed in a number of publications (e.g., *Plant et al.* [1999] estimated 200 m; *Miller and Dean* [2007] found 300 m). The erosion signal from July to December to the north of the pier features a landward shoreline anomaly of about 5 m that progresses away from the pier at approximately 100 m per month. An equivalent but weaker winter erosive signal on the south propagates away from the pier at about 50 m/month.

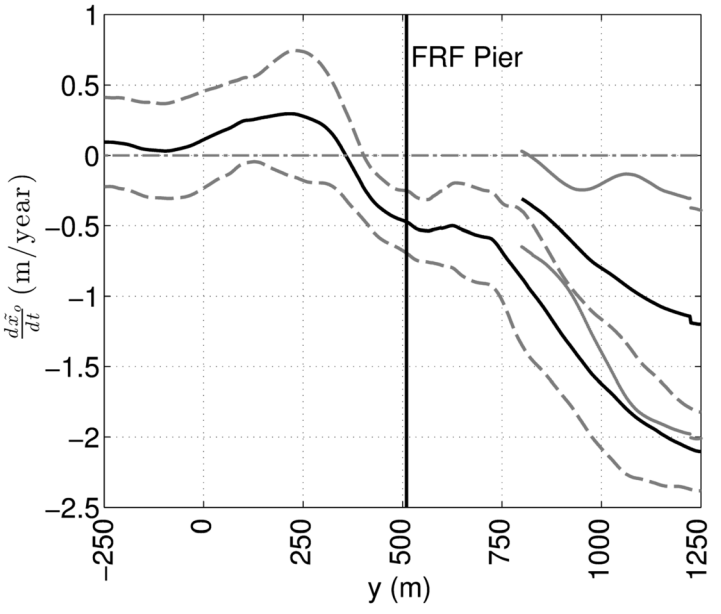


**Figure 9.** Slopes from the linear regression as a function of alongshore locations and 95% confidence levels (solid and dash gray lines) for the 26 and 16 year data sets (short lines correspond to the 26 year data set). The FRF pier location (thick black line) is plotted for reference.

Alongshore-averaged power spectra for both data sets are shown in Figure 6 (right). The dominant characteristic of these spectra is the linear

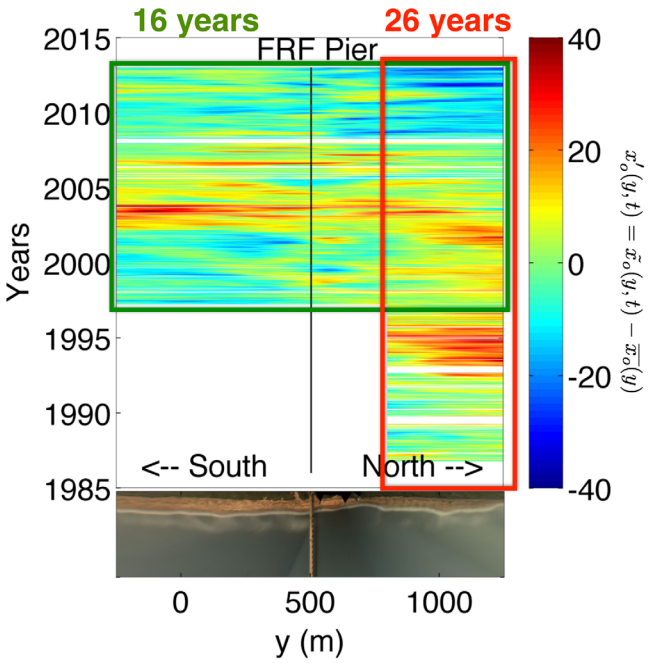


**Figure 10.** Space-time plot of the shoreline deviations (m) as a function of alongshore location and time. Cold colors indicate a erosive position and hot colors accretionary deviations of shoreline position. The FRF pier is shown by the black line in the middle of the plot and the data sets for 26 years and 16 years are illustrated by the red and green rectangles, respectively. For reference, a rectified timex image is provided at the bottom. White indicates regions of no data.

decay (in a log-log format) of variance with frequency, consistent with a power law format, $f^{-\alpha}$. From the least-squares slope fit for the 26 year data set, the coefficient of energy, $\alpha$, is 1.56 $\pm$ 0.02 with an $R^2$ of 0.82, while for the 16 year data set is $\alpha$ was found to be 1.74 $\pm$ 0.015 with an $R^2$ of 0.93.

The annual cycle is apparent in both data sets while the semiannual harmonic (2 cycles/yr), present in the wave forcing records, is not obvious in the shoreline response. The spectra also show interannual energy located in broad peaks such as the one centered on the period of 7 years (26 years data set) and one centered at 4 years in the PSD for the 16 year data set. There is also a narrow peak at the period of 14.78 days for the 26 years spectra that is not apparent in the shorter data set, 16 years. This is actually a frequency alias due to the once-per-day data sampling strategy used between the years of 1986–1993. This sampling rate implies in an undersampling of the M2 tide with a predicted alias to a period of 14.78 days, the same as observed. Despite the attempted removal of tidal effects in computing $\hat{x_o}$, the assumption of constant beach slope was not perfect and aliasing was introduced. This problem was solved by the change to hourly sampling in 1993.

The spectra were partitioned into each of the four frequency bands defined previously and the amplitudes and percentages explained by each band computed (Table 3). In sharp contrast to the wave forcing data that was dominated by the weather band (60–74%) with only a few percent interannual influence, the shoreline response is dominated by interannual variability (66–71%), with the weather band only contributing 3–5% of the signal.

Longshore variability of spectral characteristics over the 16 years of full longshore coverage were examined using a space-frequency plot, or frequency stack, of the power spectra in Figure 12 and as band-integrated equivalent amplitudes in Figure 13. The four frequency bands in the frequency stack are illustrated by dashed black lines with a dashed gray line showing the semiannual harmonic. We again see that most of the energy occurs at interannual frequencies for all the $y$ locations, although with a 40% drop in amplitude (60% in variance) near the pier, a variation in amplitude of over 4 m. The annual signal is evident in all alongshore locations but with energy reduced by a factor of nearly four in the vicinity of the pier (a 3 m reduction compared to more distant locations). The semiannual cycle (period of 6 months, the gray line) is also visible, but is mostly concentrated near the pier (400 $\leq y \leq$ 605 m) and well north of pier. Intra-annual signals present the opposite variation of the interannual with a higher amplitude near the pier and approximately 2 m difference between the north and south sides. The energy contained in the weather band is small despite its dominance of the wave forcing and is relatively longshore-uniform.

### 3.2. Spatial Variability

To investigate the longshore variability of the shoreline over time, EOF analysis was applied. Here, just the data set from the 16 years record will be discussed, since it covers the full 1500 m alongshore and shows clearly the influence of the pier. Figure 14 shows the spatial weights and the time series of EOF scores for the first four EOFs that summed together explain 87.53% of the variance.

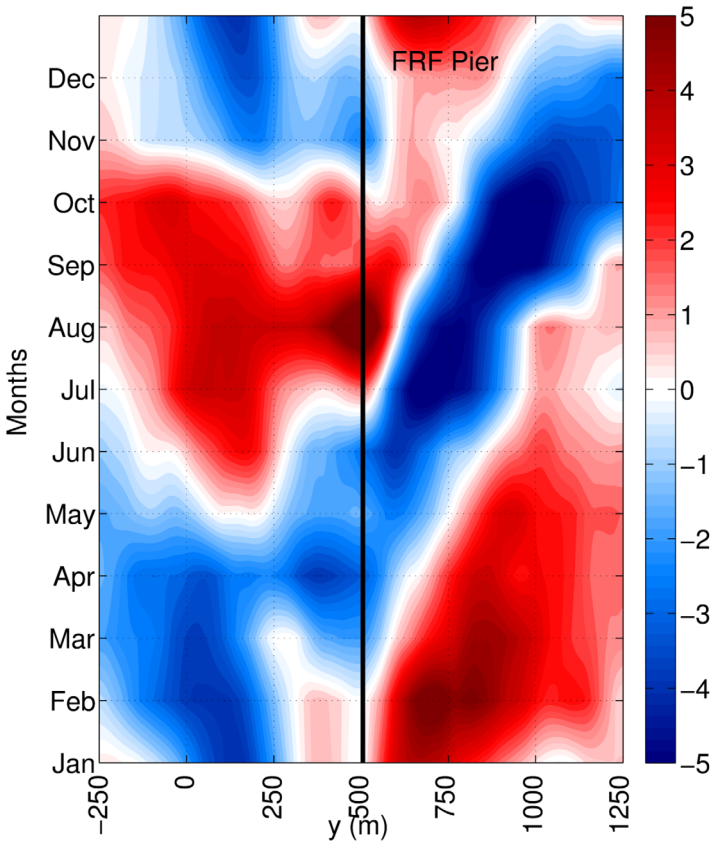


**Figure 11.** Monthly averaged shoreline deviations (m). Hot colors indicate accretion (seaward positions) and cold colors indicate erosion (landward position).

The first EOF explains 48.79% of the variance. Since the EOF weights (Figure 14a) are essentially alongshore-uniform, this mode represents the cross-shore movement (landward-seaward) of the shoreline. The resulting scores for this mode look like the alongshore-averaged shoreline time series (Figure 8), with accretion between the years 2001–2004 and erosion from 2007 to 2009, and this EOF shows the overall of erosion and accretion response. The EOF time series does not exhibit an annual cycle, but is dominated by an interannual, roughly decadal, period.

The second EOF explains 26.13% of the variance and shows alternating accretion and erosion on each side of the pier and a node point around the pier location. EOF 2 shows a strong annual cycle. There is a shift in 2002–2003 where the beach seems to change from broad to narrower in the north, never recovering the position that it had before 2002. This pattern is also obvious in the deviation time stack, Figure 10.

EOF 3 explains 7.01% of the variability and represents changes in the embayment on the north side of the pier centered at $y = 750$ m. Like EOF 2, the time series for the EOF 3 seems to have a strong annual signal, but with a different phase from EOF 2. The combination would result in an annual alongshore shift but modified in the vicinity of the pier. EOF 4 seems to be a localized response around the pier (between $250 \leq y \leq 750$ m, i.e., a length of 500 m). This mode explains 5.60% of the variance and may result in variations in the way waves refract around the pier pilings or away from the deep trench underneath the pier.

Table 4 presents the percentage of variance explained by each EOF mode for each of the four frequency bands. The percentage of the interannual cycle decreased from mode 1 and 2 to mode 3 and 4, but the intra-annual band increased in the opposite way. We confirm that the annual cycle was absent for mode 1, i.e., the alongshore-averaged shoreline, only explaining 0.14% of the variance. Mode 3 explains 30.39%, 24.11%, and 37.77% of the interannual, annual, and semiannual frequency bands, respectively, consistent with its role modifying the near-pier shape of the shoreline.

**Table 3.** Alongshore-Averages of Amplitudes and Percentages of Variance Explained for Each Frequencies Bands for the Shoreline Response Data

| | 16 Years | | 26 Years | |
|---|---|---|---|---|
| Cycles | Amplitude (m) | % Variance | Amplitude (m) | % Variance |
| Interannual | 11.08 | 66.13 | 13.79 | 70.44 |
| Annual | 3.02 | 5.51 | 2.85 | 4.18 |
| Intra-annual | 6.66 | 24.82 | 7.17 | 20.22 |
| Weather | 2.53 | 3.55 | 3.68 | 5.0 |

### 3.3. Cross-Spectrum Between Forcing and Response

To evaluate the relation between wave forcing and shoreline response, cross-spectral analysis was run between the shoreline data at each longshore location and the wave parameters ($H_{sig}$ and

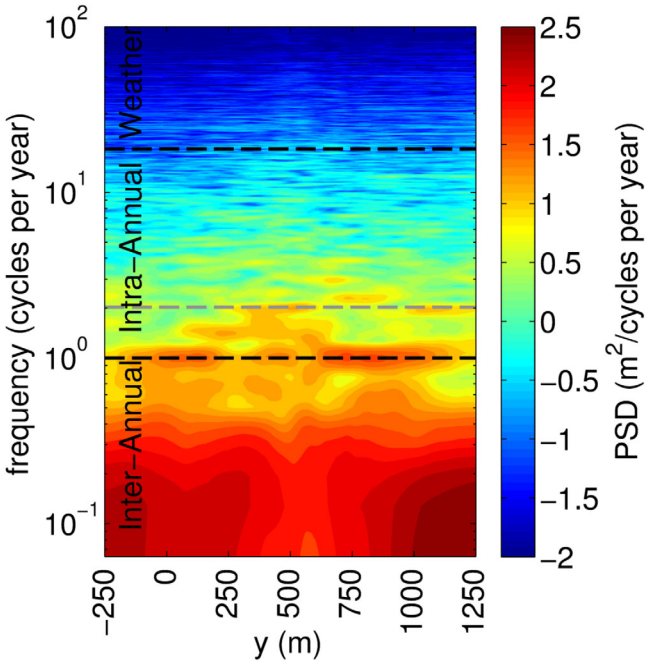


**Figure 12.** Space-frequency plot of the power spectrum (dof = 10) for the 16 years data. The dashed black lines represent the division between the cycles: weather and intra-annual (20 days line), intra-annual and interannual (1 year line, which also represent the annual cycle). The dashed gray line corresponds to two cycle per year, i.e., the semiannual harmonic. Hot colors correspond to higher variance and cold colors to lower variance values.

$P_y$). The coherence-squared results for the 16 year record are shown in Figure 15. Here again we will only show the results for the 16 years to maximize longshore coverage, but the outcomes for the 26 year record had the same conclusions for the equivalent area ($800 \leq y \leq 1250$ m).

Despite the small fraction of the overall variance explained by the annual cycle of forcing over the shoreline data, the coherence in this band shows a strong relation to $H_{sig}$ and $P_y$ (Figure 15). The coherence between wave height and the shoreline is showed on the left plot from that figure. Coherence in the annual cycle band is nearly alongshore uniform except for the region around the pier where the coherence decays from 0.8 to 0.6 but it is still significant. On the other hand, we observe a high coherence in the semiannual frequency band in the region around the pier, between $200 \leq y \leq 800$ m. The other high frequencies (shorter than the semiannual period and including the weather band of 2 days to 20 days) in this and the other plot show peaks with significant coherence; however, they are spread over longshore locations and represent only 3.55% of the total variance on the shoreline data.

The coherence between the alongshore wave energy flux and the shoreline, shown in Figure 15 (right), shows patterns that are different from the previous. The annual signal is not longshore uniform, with high coherence absent from pier region. There is significant coherence on the south part between $-250 \leq y \leq 200$ m, and sporadically on the north side. In the semiannual band, the coherence is more similar with the previous forcing, where most of the coherence is around the pier. The main difference between this and the previous plot is the high coherence in the interannual band for the north side of the beach, suggesting the importance of longshore transport to interannual variability in this part of the beach. We also see a coherence peak around the pier for the interannual cycle.

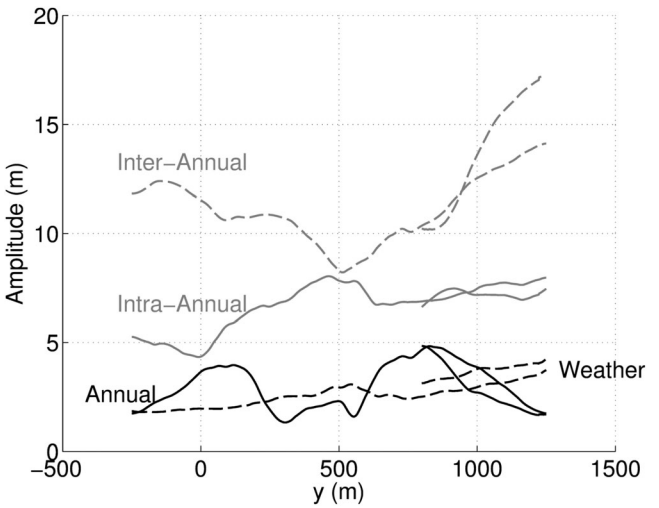


**Figure 13.** Amplitudes ($Amp = \sqrt{2Var}$) as a function of alongshore positions for each the four bands studied: interannual (dashed gray line), intra-annual (solid gray line), annual (solid black line), and weather (dashed black line).

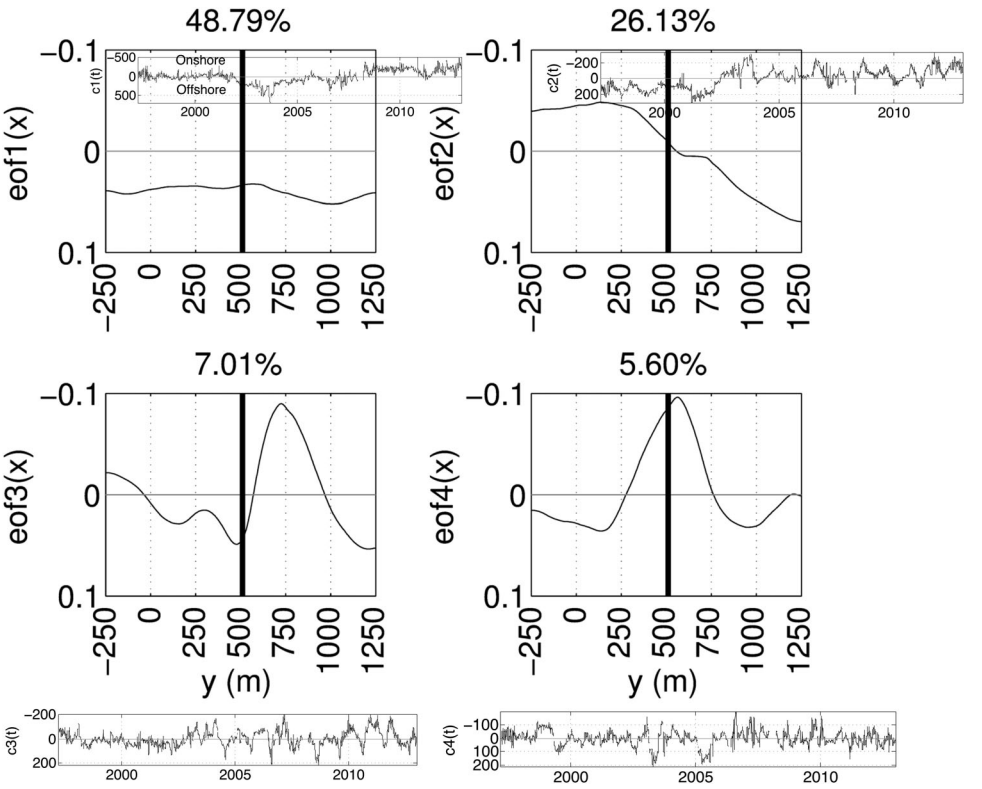


**Figure 14.** EOF weights and the respectively time series of EOF scores (c1(t), c2(t), etc) for the first four modes. The pier was plotted for reference.

To further evaluate the relation between wave forcing and shoreline response, the EOF scores of the two first modes were also compared with wave height and $P_y$ using the cross-spectra analysis. The four plots of Figure 16 presents the results from the coherence and phase between the wave height (top) and $P_y$ (bottom) with the first (left) and second (right) EOF scores. The first EOF shows no coherence with wave height in the annual frequency band but significant coherence (squared coherence of 0.60) at the semiannual cycle between 6 and 7 months. At the higher frequencies (weather band), there are peaks over the 95% confidence level; however, the overall of variance explained is small compared to lower frequencies. Thus, the mean cross-shore movement of the shoreline is influenced more by intra-annual variations in wave height than by the annual cycle. The phase is negative, thus an increase of the wave height will cause an erosion of the shoreline (since they have opposite signs). The second EOF shows strong coherence (coherence-squared = 0.8) in the annual band, hence changes in wave height over the year will cause an opposite result on either side of the pier, erosion on one side and accretion on the other. This was also found on Figure 11.

The coherence of the alongshore component of wave energy flux with the EOF scores is shown in Figure 16 (bottom). The first mode and the alongshore transport show coherence in the semiannual harmonic (6–7 month) with a squared coherence of about 0.60. A small portion of the interannual band is also coherent ($cor^2 \sim 0.5$). Mode 2 exhibits a significant coherence ($\sim$0.65) with $P_y$ at the annual band, reflecting the annual change in longshore transport and its pier blocking, as represented by EOF 2. There is also significant coherence ($\sim$0.73) at interannual frequencies.

**Table 4.** Percentages of Variance Explained by Each of the Four EOFs for Each of the Four Frequency Band

| Cycles | PC 1 % Var | PC 2 % Var | PC 3 % Var | PC 4 % Var |
|---|---|---|---|---|
| Interannual | 58.41% | 59.22% | 30.39% | 33.74% |
| Annual | 0.14% | 10.80% | 24.11% | 9.40% |
| Intra-annual | 14.95% | 11.68% | 37.77% | 48.55% |
| Weather | 3.47% | 2.22% | 4.10% | 6.48 % |

## 4. Discussion

Perhaps the most striking result of this work is documentation of the differences between wave forcing and shoreline response. The

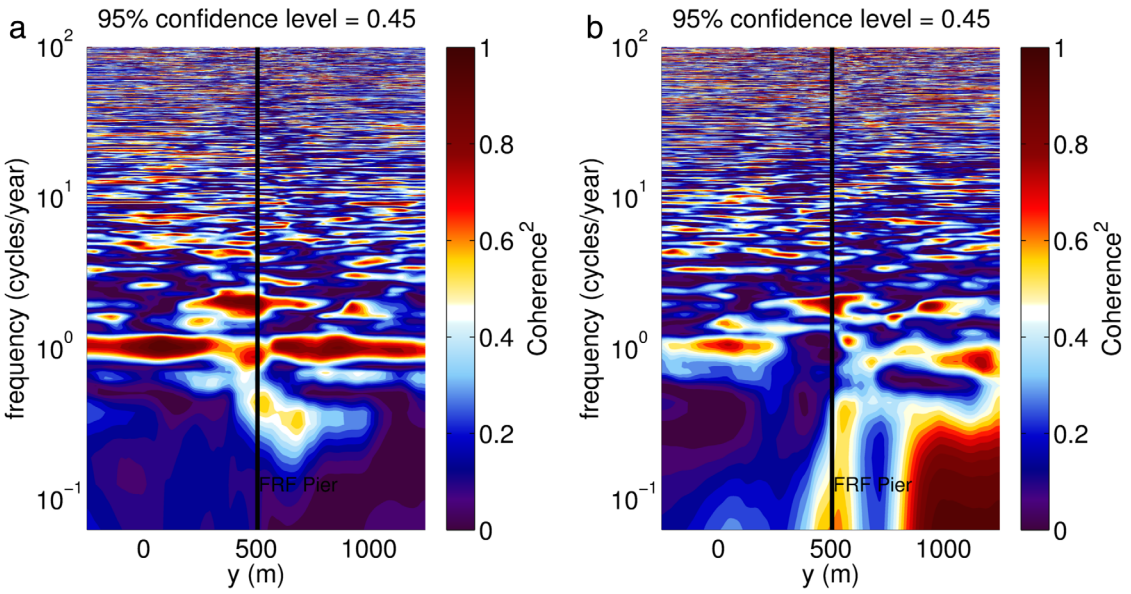


**Figure 15.** Coherence squared between shoreline data (16 years data set) and wave height (left) and alongshore wave energy flux (right). The white color corresponds to the 95% confidence level. Hot colors correspond to high coherence and cold colors small coherence below the 95% confidence level.

majority of variance (66%) in shoreline response is at longer than annual time scales, despite the fact that less than 2% of the forcing lies at these long time scales. Similarly, the bulk of the forcing (2/3) lies in the weather band (time scales less than 20 days) but this drives only 5% or less of the shoreline variability. The mismatch between forcing and response is also evident in the spectra of the two signals. Wave forcing exhibits a flat spectrum at frequencies out to the weather band with the only features being strong annual and semiannual peaks, whereas shoreline response shows a very red spectrum that decays as approximately $f^{-5/3}$ over all measurable scales. The relevance of the $-5/3$ slope, also observed in other systems such as turbulence, is unknown but the linearity (in log-log space) of the spectral slope is striking.

The annual cycle shows a significant peak in forcing spectra although it represents only 5% for the total wave height variability. Variability at annual time scales is also present at each *y* location (Figures 11 and 6) and is coherent almost everywhere with the wave forcing (Figure 15). However, the response on the north and south sides of the pier are in opposite phase (erosion versus accretion), as shown in the second EOF as well as in 11, so that the alongshore averaged shoreline response at annual time scales is not significant or coherent with the forcing. *Alexander and Holman* [2004] and *Plant et al*. [1999] also found a lack of an annual cycle over shoreline time series and sandbar locations at Duck.

*Yates et al*. [2009] and *Hansen and Barnard* [2010] investigated the relation between shoreline change and wave forcing over 5 years using GPS surveys at Torrey Pines Beach (California) and Ocean Beach (San Francisco), respectively, and found that seasonal processes dominate the shoreline changes due to seasonal variations on the wave height. While their temporal resolution was much less than the hourly to daily sampling discussed here and their record length was shorter than our 26 years, it is unclear why they were successful using a forcing-dominated model while we see such large discrepancies between forcing and response time scales. In contrast, *Hansen and Barnard* [2010] also found interannual variability in shoreline change that they associated with large bathymetric features such as large ebb tidal delta lobes located near the shoreline. *Alegria-Arzaburu and Masselink* [2010] using a 3 year record of video images on a gravel beach at Slapton Sands (UK), found an alongshore difference in the correlation between beach volume and wave climate, where the south part of the beach is dominated by a seasonal response to the wave climate, while on the middle and north parts, the shoreline response is dominated by long-term processes.

The presence of an annual cycle in shoreline response that is coherent with forcing but becomes incoherent under alongshore-averaging demonstrates the importance of the FRF research pier on local shoreline variability. The FRF site was chosen as a location of alongshore-uniform processes, well away from inlets or

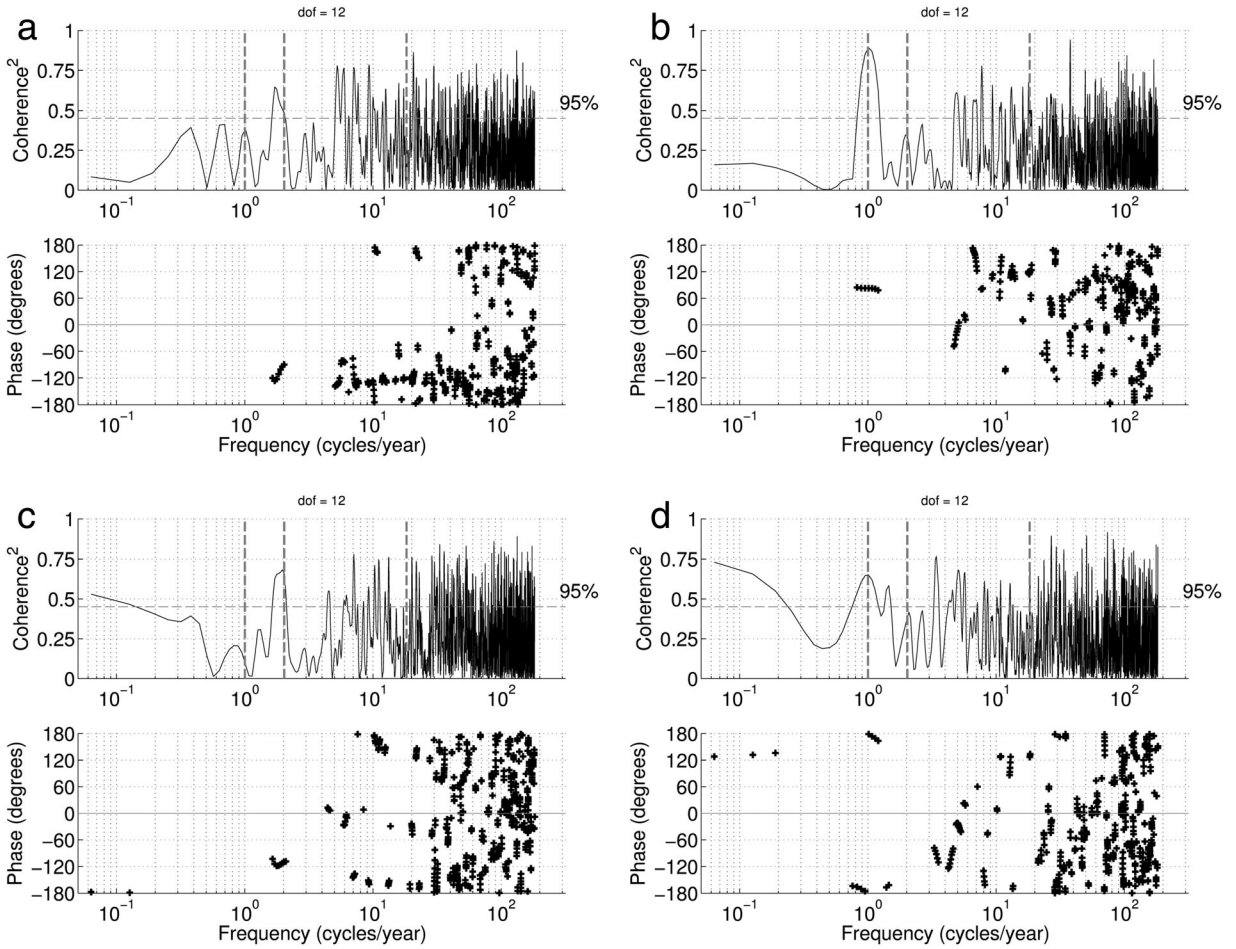


**Figure 16.** Coherence and phase between wave height (top) and $P_y$ (bottom) with the first (left) and second (right) EOF scores time series. The dashed gray lines represent the annual, semiannual, and 20 days frequencies, respectively.

other coastal interruptions. However, the presence of the constructed pier apparently causes gradients in longshore transport and associated erosion and accretion on opposite sides of the pier that alternate seasonally. A pier effect has been noted previously but the region of influence seen here of almost 500 m is about twice the values used by previous studies (e.g., *Plant et al*. [1999] estimated 200 m; *Miller and Dean* [2007] found 300 m). These seasonal pier effects are also apparently associated with the propagation of sand waves away from the pier.

The shoreline erosion trend found in this work showed no significant erosion on the south side but an erosion rate for the north side of up to 1–2 m/yr or a total change of 26–48 m in 26 years. This north side trend may be consistent with the increases in northward longshore energy flux found in Table 1. From the cumulative probability analysis of the shoreline location, it was shown that the north is more unstable than the south part and the 2% exceedance location is 15 m further landward on the north than on the south side. This analysis is a useful tool for coastal managers and engineers since it indicates the statistics of shoreline extremes.

The shoreline is one measure of beach profile variability. Previous authors have shown that the shoreline and offshore sand bars behave in a coupled way [*Van de Lageweg et al*., 2013]. While this link was not investigated in this study, it was observed that the large offshore variations in shoreline position in 1995 and 2003 (Figure 8) corresponded visually to the generation of new sand bars from the shoreline area as part of the known phenomenon of offshore propagating sand bars [e.g., *Wijnberg and Terwindt*, 1995; *Plant et al*., 1999].

This analysis relied on several site-specific parameters. The shoreline slope chosen for ASLIM was a climatological value from the literature but undoubtedly varies over time and even seasons. Since the focus of this work was on long-time scale variability, this assumption of constant slope was preferred over a fancier (and potentially more finicky) time-varying alternate. Similarly, the definition of the pier orientation varies in the literature. For example, *Miller* [1999] noted an offshore orientation of 69.7°, whereas online FRF documentation notes an angle of 71.8°. This difference will affect the mean $P_y$ values but not the variability or cross-spectral characteristics.

## 5. Conclusions

The present work examines a unique 26 year record of shoreline data and 24 year record of wave forcing from a steep beach at Duck, North Carolina. A model was developed, called ASLIM (Augmented ShoreLine Intensity Maxima) to extract the shoreline positions based on fitting the band of high light intensity (distinct shore break) in time exposure images to a local Gaussian fit with a subsequent Kalman filter to reduce noise and uncertainty. The ASLIM model showed good agreement with ground truth survey data.

The shoreline response was surprising in several ways. The shoreline change at long-time scales dominates seasonal variability, despite that wave forcing had only 2% variance at interannual frequencies. Most of the oscillations were explained by periods longer than the annual cycle, while wave forcing is dominated by shorter periods (weather band). This result was not expected since from wave forcing it would have been expected that the shoreline response should similarly lack interannual variability, but we found it to be dominated by this scale. However, there are annual oscillations that are coherent with wave forcing that deserves further explanations. The power spectrum of alongshore-mean shoreline position revealed no significant annual peak and, in contrast to the flat spectrum of wave forcing, the energy decay showed a remarkably straight power law decay of $f^{-5/3}$ down to decadal time scales. The shoreline response seems to be more directly coupled with the sand bars dynamics than with the wave forcing; however, this link was not investigated here, and need further investigations.

The pier was found to have a significant influence on shoreline behavior. It restricts seasonal longshore transport from the south (summer) and north (winter) sides, resulting in a seasonally reversing sediment accumulation on the updrift side. Thus, there is everywhere a significant annual peak in shoreline variability that is coherent with the annual forcing but becomes insignificant in the longshore-average. Erosion signals on the downdrift side of the pier were found to propagate away from the pier at 100 m/month. A shoreline erosion trend that was found only on the north side of the pier may be related to the trend found in the alongshore transport, $P_y$, that it is increasing toward the north and is being blocked by the pier.

**Acknowledgments**

The authors would like to thank John Stanley, without whose help none of this would have happened, and the Field Research Field (FRF) team for their long-term professional work in advancing nearshore science and for access to the wave, tide, and survey data (http://frf.usace.army.mil). We would like to thank Piero Mazzini for helpful discussions and comments. Support for Cassia Pianca was provided by São Paulo Research Foundation (FAPESP—2010/13083-3). Support for Rob Holman was provided by the Office of Naval Research, Award number N000141010932. Eduardo Siegle is sponsored by a CNPq research fellowship. Finally, we would like to thank the two anonymous reviewers for providing detailed reviews and the editor Thomas Herbers for providing useful comments that improved our manuscript. The data used in this publication are available by contacting Rob Holman (holman@coas.oregonstate.edu).

## References

Aarninkhof, S. G. J., I. L. Turner, T. D. Dronkers, M. Caljouw, and L. Nipius (2003), A video-based technique for mapping intertidal beach bathymetry, *Coast. Eng.*, *49*, 275–289.

Alegria-Arzaburu, A. R., and G. Masselink (2010), Storm response and beach rotation on a gravel beach, Slapton Sands, U.K., *Mar. Geol.*, *278*, 77–99.

Alexander, P. S., and R. A. Holman (2004), Quantification of nearshore morphology based on video imaging, *Mar. Geol.*, *208*, 101–111.

Boak, E. H., and I. L. Turner (2005), Shoreline definition and detection: A review, *J. Coast. Res.*, *21*(4), 688–703.

Chen, C., P. Malanotte-Rizzoli, J. Wei, R. C. Beardsley, Z. Lai, P. Xue, S. Lyu, Q. Xu, J. Qi, and G. W. Cowles (2009), Application and comparison of Kalman filters for coastal ocean problems: An experiment with FVCOM, *J. Geophys. Res.*, *114*, C05011, doi:10.1029/2007JC004548.

Crowell, M., S. P. Leatherman, and M. K. Buckley (1991), Historical shoreline change: Error analysis and mapping accuracy, *J. Coast. Res.*, *7*(3), 839–852.

Hansen, J. E., and P. L. Barnard (2010), Sub-weekly to interannual variability of a high-energy shoreline, *Coast. Eng.*, *57*, 959–972.

Hapke, C. J., D. Reid, B. Richmond, P. Ruggiero, and J. List (2006), National assessment of shoreline change part 3: Historical shoreline changes and associated coastal land loss along the sandy shorelines of the California Coast, *U.S. Geol. Surv. Open File Report* 2006-1219, 72 pp.

Holland, K. T. (1998), Beach cusp formation and spacings at Duck, USA, *Cont. Shelf Res.*, *18*, 1081–1098.

Holland, K. T, R. A. Holman, T. C. Lippmann, J. Stanley, and N. Plant (1997), Practical use of video imagery in nearshore oceanographic field studies, *J. Ocean Eng.*, *22*, 81–92.

Holman, R., N. Plant, and T. Holland (2013), cBathy: A robust algorithm for estimating nearshore bathymetry, *J. Geophys. Res. Oceans*, *118*, 2595–2609, doi:10.1002/jgrc.20199.

Holman, R. A., and J. Stanley (2007), The history and technical capabilities of Argus, *Coast. Eng.*, *54*, 477–491.

Kingston, K. S. (2003), *Applications of complex adaptive systems, approaches to coastal systems, Ph.D. thesis*, Inst. of Mar. Sci., Univ. of Plymouth, Plymouth, U. K.

Komar, P. (1998), *Beach Processes and Sedimentation*, 2nd ed., Prentice Hall, 544 pp.

Long, J. W., and N. G. Plant (2012), Extended Kalman filter framework for forecasting shoreline evolution, *Geophys. Res. Lett.*, *39*, L13603, doi:10.1029/2012GL052180.
Madsen, A. J., and N. G. Plant (2001), Intertidal beach slope predictions compared to field data, *Mar. Geol.*, *173*, 121–139.
Miller, H. (1999), Field measurements of longshore sediment transport during storms, *Coast. Eng.*, *36*(4), 301–321.
Miller, J. K., and R. G. Dean (2004), A simple new shoreline model, *Coast. Eng.*, *51*, 531–556.
Miller, J. K., and R. G. Dean (2007), Shoreline variability via empirical orthogonal function analysis part I: Temporal and spatial characteristics, *Coast. Eng.*, *54*, 111–131.
Min V & W (1990), Coastal defense after 1990, a policy choice for coastal protection, 1st Coastal Policy Document, Ministry of Transport, Public Works and Water Management, The Hague, N. L.
Moore, L. J. (2000), Shoreline mapping techniques, *J. Coast. Res.*, *16*(1), 111–124.
Morton, R. A., (1996), Geoindicators of coastal wetlands and shorelines, in *Geoindicators: Assessing Rapid Environmental Changes in Earth Systems*, edited by A. R. Berger and W. J. Iams, pp. 207–230, A. A. Balkema, Rotterdam.
Morton, R. A., M. P. Leach, J. G. Paine and M. A. Cardoza, (1993), Monitoring beach changes using GPS surveying techniques, *J. Coast. Res.*, *9*(3), 702–720.
Plant, N. G., and R. A. Holman (1997), Intertidal beach profile estimation using video images, *Mar. Geol.*, *140*, 1–24.
Plant, N. G., R. A. Holman, M. H. Freilich, and W. A. Birkemeier (1999), A simple model for interannual sandbar behavior, *J. Geophys. Res.*, *104*(C7), 15,755–15,776.
Plant, N. G., S. G. J. Aarninkhof, I. L. Turner, and K. S. Kingston (2007), The performance of shoreline detection models applied to video imagery, *J. Coast. Res.*, *23*(3), 658–670.
Ruggiero, P., J. Cote, G. M. Kaminsky, and G. Gelfenbaum (1999), Scales of variability along the Columbia River littoral cell, edited by Nicholas C. Kraus and William G. McDougal, in *Proceedings of the 4th International Symposium on Coastal Engineering and Science of Coast Sediment Processes*, pp. 1692–1707, ASCE, Hauppauge, N. Y.
Ruggiero, P., G. M. Kaminsky, and G. Gelfenbaum (2003), Linking proxy-based and datum-based shorelines on a high-energy coastline: Implications for shoreline change analyses, *J. Coast. Res.*, *38*, 57–82.
Sallenger, A. H., W. Krabill, J. Brock, R. Swift, M. Jansen, S. Manizade, B. Richmond, M. Hampton, and D. Eslinger, (1999), Airborne laser study quantifies El Nino-induced coastal change, *EOS, Trans. AGU*, *80*(8), 92–93.
Smith, A. W. S., and L. A. Jackson (1992), The variability in width of the visible beach, *Shore Beach*, *60*(2), 7–14.
Stauble, D. K, (1992), Long-term profile and sediment morphodynamics: Field Research Facility case history, *Tech. Rep. CERC-92-7*, Coast. Eng. Res. Cent. Vicksburg, Miss.
Stockdon, H. F., A. H. Sallenger, J. H. List, and R. A. Holman, (2002), Estimation of shoreline position and change using airborne topographic Lidar data, *J. Coast. Res.*, *18*(3), 502–513.
Turner, I., V. Leyden, G. Symonds, J. McGrath, A. Jackson, T. Jancar, S. Aarninkhof, and I. Elshoff, (2001), Comparison of observed and predicted coastline changes at the gold coast artificial (surfing) reef, Sydney, Australia, edited by B. L. Edge, in Coastal Engineering 2000: Proceeding of the 27th International Conference on Coastal Engineering (Sydney, Australia, ASCE), pp. 1836–1847.
Van de Lageweg, W. I., K. R. Bryan, G. Coco, and B. G. Ruessink, (2013), Observations of shoreline-sandbar coupling on an embayed beach, *Mar. Geol.*, *344*, 101–114.
Wijnberg, K. M., and J. H. J. Terwindt, (1995), Extracting decadal morphological behaviour from high-resolution, long-term bathymetric surveys along the Holland coast using eigenfunction analysis, *Mar. Geol.*, *126*(1–4), 301–330.
Wilson, G. W., H. T. Ozkan-Haller, and R. A. Holman, (2010), Data assimilation and bathymetric inversion in a two dimensional horizontal surf zone model, *J. Geophys. Res.*, *115*, C12057, doi:10.1029/2010JC006286.
Yates, M. L., R. T. Guza, and W. C. O'Reilly (2009), Equilibrium shoreline response: Observations and modeling, *J. Geophys. Res.*, *114*, C09014, doi:10.1029/2009JC005359.